This article has been accepted for publication in IEEE Transactions on Medical Imaging. This is the author's version which has not been fully edited and content may change prior to final publication. Citation information: DOI 10.1109/TMI.2025.3643618

Multifocal Optical-resolution Photoacoustic Microscopy with a Masked Single-element Transducer

Xiaofei Luo, Rui Cao, Peng Hu, Yilin Luo, Yushun Zeng, Yide Zhang, Manxiu Cui, Qifa Zhou, Geng Ku, and Lihong V. Wang, *Fellow, IEEE*

***Abstract*—Optical-resolution photoacoustic microscopy (OR-PAM) can visualize cellular-level wavelength-dependent optical absorption with high resolution and sensitivity. However, the imaging speed of OR-PAM has been limited by the laser repetition rate due to the point-by-point scanning of a focused laser beam. To overcome this limitation, we propose multifocal optical-resolution photoacoustic microscopy (MOR-PAM) with a single-element ultrasonic transducer, leveraging the diffractive optical element (DOE) and a custom-designed encoding acoustic mask. The DOE generates 8 focal spots of 3 μm diameter. The acoustic mask was designed to encode photoacoustic signals from different focal spots. MOR-PAM achieved an 8-fold increase in imaging speed compared to conventional OR-PAM with the same laser repetition rate. We demonstrated the MOR-PAM using a 266 nm laser at 10 KHz, providing solutions for rapid OR-PAM beyond the laser repetition rate in a cost-effective way. The proposed method can be applied to versatile OR-PAM configurations and enable new applications where high-speed imaging is critical.**

***Index Terms*— Structural illumination, Compressed sensing, Photoacoustic microscopy.**

I. INTRODUCTION

OPTICAL-RESOLUTION photoacoustic microscopy (OR-PAM) is a widely used imaging technique in various biomedical applications [1-6], attributed to the capability of providing high-resolution and high-sensitivity visualization of wavelength-dependent optical absorption at the cellular level [7-11]. However, the imaging speed of high-resolution laser scanning microscopy, including OR-PAM, has been limited due to the requirement of point-by-point scanning using a focused laser beam [12, 13]. Acceleration of the imaging speed has been achieved by using lasers with higher pulse repetition rates (PRRs) and rapid beam steering with mirrors on piezo scanners or microelectromechanical scanners [14, 15]. These approaches enable faster scanning rates but are still limited to laser PRR.

To address this problem, researchers have demonstrated multiple excitation spots with an ultrasonic array to get high-resolution imaging at a speed beyond laser PRRs, utilizing photoacoustic computed tomography (PACT) reconstruction to resolve different excitation spots [16-18]. However, PACT requires complex and expensive multi-channel detection and data acquisition. Those methods improved the imaging speed with high system development. To fill the gap for low-cost and high-speed photoacoustic imaging system, researchers have developed single-detector photoacoustic imaging [19-21], based on spatiotemporal encoded ultrasound signals via an ergodic relay (ER) or a chaotic cavity [22, 23]. Combined with optical foci arrays and appropriate reconstruction strategies, this acoustic encoding strategy can also achieve optical-resolution photoacoustic imaging [21]. But they usually require object-dependent calibration, which can be time consuming and inconvenient. Moreover, long-term stability is difficult to achieve in various environments due to the sensitivity to boundary conditions. Recent studies have introduced improved solutions that enable single-shot imaging without object-dependent calibration [24-26]. However, the reliance on long acoustic delay lines results in significant attenuation of high-frequency signals.

In this study, we developed multifocal optical-resolution photoacoustic microscopy (MOR-PAM) using a single-element transducer and acoustic encoding mask to achieve speed improvement. The MOR-PAM system utilizes a diffractive

L.V.W. was sponsored by the United States National Institutes of Health grants R01 EB028277 and R35 CA220436 (Outstanding Investigator Award). R.C. was sponsored by the United States National Institutes of Health grants R00 EB034298 and T32 EB027629. Y.Z. was sponsored by the United States National Institutes of Health grants K99 EB035645. (*Corresponding author: Lihong V. Wang.*)

X. L., R. C., P. H., Y. L., Y. Z., M. C., G. K. and L.V.W. are with the Caltech Optical Imaging Laboratory, Andrew and Peggy Cherng Department of Medical Engineering and Department of Electrical Engineering, California Institute of Technology, Pasadena, CA 91125 USA. (xfl@csust.edu.cn; LVW@caltech.edu).

X. L.'s present address is the Mechanical and Vehicle Engineering Department of Changsha University of Science and Technology. Present address for R. C. is Department of Biomedical Engineering at Case Western Reserve University.

Y. Z. and Q. Z. are with the Alfred E. Mann Department of Biomedical Engineering, University of Southern California, Los Angeles, CA, USA.

Y. Z. and Q. Z. are also with the USC Roski Eye Institute, University of Southern California, Los Angeles, CA, USA.

(*These authors contributed equally: Xiaofei Luo, Rui Cao.*)

Authorized licensed use limited to: CALIFORNIA INSTITUTE OF TECHNOLOGY. Downloaded on December 16,2025 at 17:50:50 UTC from IEEE Xplore. Restrictions apply.
© 2025 IEEE. All rights reserved, including rights for text and data mining and training of artificial intelligence and similar technologies. Personal use is permitted, but republication/redistribution requires IEEE permission. See https://www.ieee.org/publications/rights/index.html for more information.

This article has been accepted for publication in IEEE Transactions on Medical Imaging. This is the author's version which has not been fully edited and content may change prior to final publication. Citation information: DOI 10.1109/TMI.2025.3643618

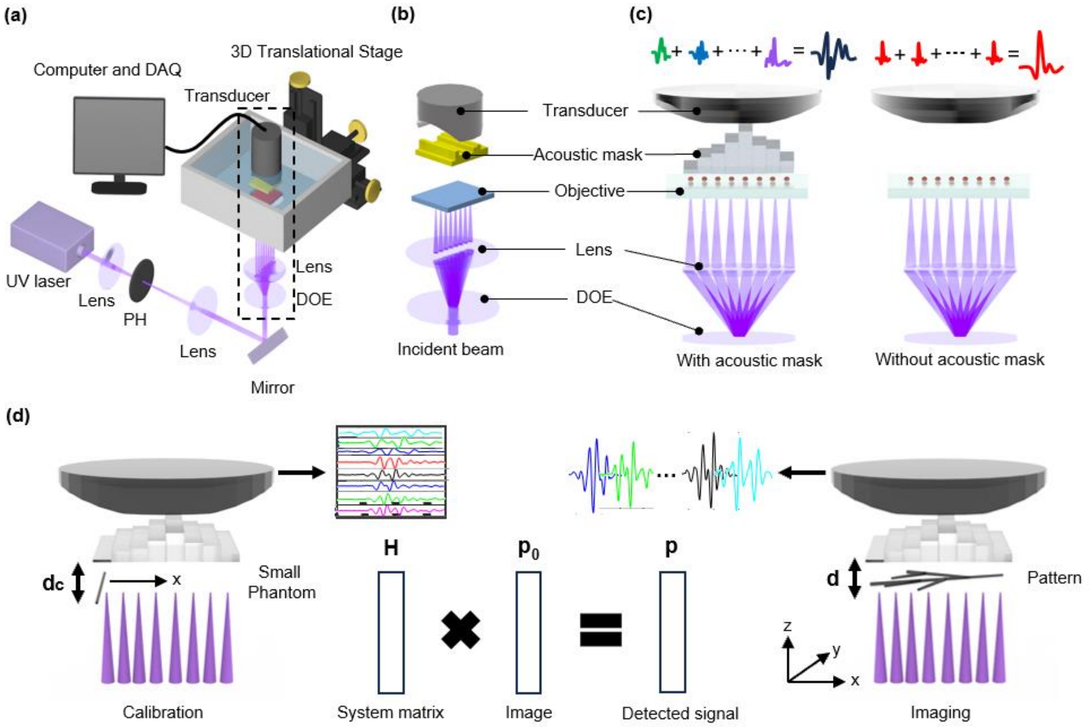

Fig. 1 Schematic of MOR-PAM. (a) Details of the MOR-PAM system configuration. (b) Close-up view of the black dashed box in a. (c) Comparison of MOR-PAM with (left) and without the acoustic mask (right). Without a mask (right), overlapped photoacoustic signals from different focal spots cannot be differentiated. (d) The calibration of MOR-PAM signals and image reconstruction via FISTA. The vector $\mathbf{P_0}$ is formed by the initial pressures, the vector $\mathbf{P}$ is formed by discretized signals detected by the transducer and $\mathbf{H}$ represents the system matrix.

optical element (DOE) and an objective lens to generate multiple focused laser beams. The photoacoustic (PA) signals propagate through the encoding acoustic mask and are received by the ultrasonic transducer with minimal attenuation. As a thin glass plate, the DOE can be easily integrated into an existing optical system to transform the conventional OR-PAM into MOR-PAM without a complicated and expensive setup [27, 28]. Customized fast iterative shrinkage-thresholding algorithm (FISTA) is developed to decode mixed PA signals for image reconstruction [29]. To demonstrate the feasibility and evaluate performance, a hair phantom and a leaf skeleton phantom were imaged using MOR-PAM with a 266 nm laser at 10 kHz. Our MOR-PAM approach enables high-speed OR-PAM with reduced hardware complexity and costs.

II. METHODS

A. MOR-PAM system

Our MOR-PAM system consists of an Nd:YLF Q-switched 266 nm nanosecond pulsed laser (QL266-010-O, CrystaLaser) to illuminate the object, an acoustic mask, and a customized cylindrical focused transducer (focal length of 19 mm, central frequency of 19 MHz, and -6 dB two-way bandwidth of 13–25 MHz). The reconfigurable I/O device (PCIE-6323, National Instruments) with a customized LabVIEW program (National Instruments) was used to control and synchronize laser pulses, motor movements, and data acquisition (Fig. 1a). The 266 nm laser has a pulse repetition rate of 10 kHz with 2 ns pulse duration. The laser beam was expanded by a pair of plano-convex lenses and spatially filtered by a 15 µm high-energy pinhole (900PH-15, Newport) before the DOE (HOLO/OR). The MOR-PAM image was acquired by scanning the water-immersed sample mounted onto a customized 3D scanner consisting of three step motors (PLS85, PI Micos). The acoustic mask was placed 2 mm away from the ultrasonic transducer to encode PA signals before detection. The detected PA signal was amplified by two low-noise amplifiers (ZFL-500LN+, Mini-Circuits) and digitized by a data acquisition card (ATS9350, Alazar Technologies) at a sampling rate of 500 MHz. To convert conventional OR-PAM into MOR-PAM, we placed the DOE in the beam path before the objective lens to split the beam in one dimension. Using the DOE (HOLO/OR) that produces a total angular spread of 37° and an objective lens (f=60 mm, Thorlabs), the incident beam was converted to 8 focal spots along one dimension at the focal plane of the objective lens.

In our MOR-PAM system, both DOE and objective lens are commercially available at moderate cost, while the acoustic mask is fabricated from inexpensive PLA material using 3D printing. Compared to the PACT setup with transducer arrays, the overall hardware cost of our MOR-PAM system is significantly lower. The beam diameter was measured to be around 3 µm. To differentiate the PA signals from multiple focal spots detected by the cylindrical focused transducer, we placed a ladder-shaped acoustic mask in the ultrasound wave propagation path between the transducer and specimen (Fig. 1b and Fig. 1c), introducing spatial encoding of photoacoustic signals from different focal spots. The 8 focal spots are distributed in 1D and aligned with the line focus of the cylindrical-focused transducer to ensure detection sensitivity. To characterize PA signals from each focal spot for

Authorized licensed use limited to: CALIFORNIA INSTITUTE OF TECHNOLOGY. Downloaded on December 16,2025 at 17:50:50 UTC from IEEE Xplore. Restrictions apply.
© 2025 IEEE. All rights reserved, including rights for text and data mining and training of artificial intelligence and similar technologies. Personal use is permitted, but republication/redistribution requires IEEE permission. See https://www.ieee.org/publications/rights/index.html for more information.

This article has been accepted for publication in IEEE Transactions on Medical Imaging. This is the author's version which has not been fully edited and content may change prior to final publication. Citation information: DOI 10.1109/TMI.2025.3643618

reconstruction, we acquired signals from a human hair sample using each individual focal beam. The hair phantom (approximately 90 µm in diameter) was placed perpendicular to the axis of the eight laser foci, which were spaced 300 µm apart on the focal plane. Due to the narrow size of the hair compared to inter-spot spacing, only one focal beam illuminated the hair at a time during calibration. Those calibrated PA signals were used as the system matrix to characterize spatial encoding by the acoustic mask, which can be used to decode mixed PA signals. It is worth noting that the characterization is not object-dependent, and the MOR-PAM was ready for imaging different specimens after system characterization (Fig. 1d).

B. Acoustic mask

To spatially encode PA signals, we introduced location-dependent phase shifts in the transmitted waves before the transducer detection by adding an encoding acoustic mask. To ensure sufficient differences in PA signals from different focal spots with minimal impact on the signal-to-noise ratio, the mask material should have a large difference in speed of sound compared to water and low acoustic attenuation. We chose the acoustic-friendly PLA material for our acoustic mask due to its ease of fabrication via 3D printing and high accessibility. With an ultrasound attenuation of 0.231 dB at 1 MHz over a 1 mm propagation distance, PLA exhibits low sound absorption.

Through the K-wave toolbox in MATLAB [27], we conducted simulations on shape and dimension of the mask. In the simulation, we used the sound velocity of 1480 m/s and density of 1000 kg/m^3 for water, the sound velocity of 2200 m/s and density of 1240 kg/m^3 for PLA mask, with the transducer central frequency of 20 MHz. A correlation matrix for eight signals under various parameters is analyzed to evaluate encoded signals for optimized mask parameters. The Pearson correlation coefficient measures the similarity between two signals, with a value of 1 indicating a perfect positive correlation and 0 indicating no correlation. Through simulation, the mask parameters achieving the minimum correlation coefficients are selected as the width and thickness of each micro ladder step of the mask. Ultimately, upon validating the optimal mask design, the PLA mask is 3D printed (CraftBot Plus, Ultimaker).

C. Fabrication of the ultrasonic transducer

A lithium niobate (LNO) single crystal (Boston Piezo-optics) ultrasonic transducer was manufactured and used in this study because of its superior sensitivity in high-frequency ultrasound detection. The 20 MHz LNO single crystal was sputtered with Au/Cr (100 nm/50 nm) on both sides as electrodes and then diced as a square element with an aperture size of 14.9 mm × 14 mm via a dicing saw (Tcar 864-1, Thermocarbon). A customized metal housing was cut for holding and electrical shielding. The diced LNO-element was fixed into the metal housing using epoxy to fill the gaps between the LNO-element and the metal housing edges for electrical isolation. For the final ground connection, the Au/Cr (100 nm/50 nm) electrode was sputtered again onto the transducer surface to conduct the LNO-element and the metal housing. A 15 µm perylene C was coated on the whole transducer as a matching layer and a water-proof shield by parylene coater (Specialty Coating Systems, Fig. 2a).

The time-domain pulse/echo response of the transducer was characterized as shown in Fig. 2b. A flat metal block was positioned in front of the transducer to serve as the acoustical reflector. Electrical pulses generated by the ultrasound pulse/receiver (DPR300, JSR Ultrasonics) stimulated the transducer element, while the ensuing signal was recorded using a digital oscilloscope (MSO54, Tektronix). The transducer was immersed in a tank of water during the measurement. The Fourier transform was applied to derive the spectrum of the transducer (Fig. 2c).

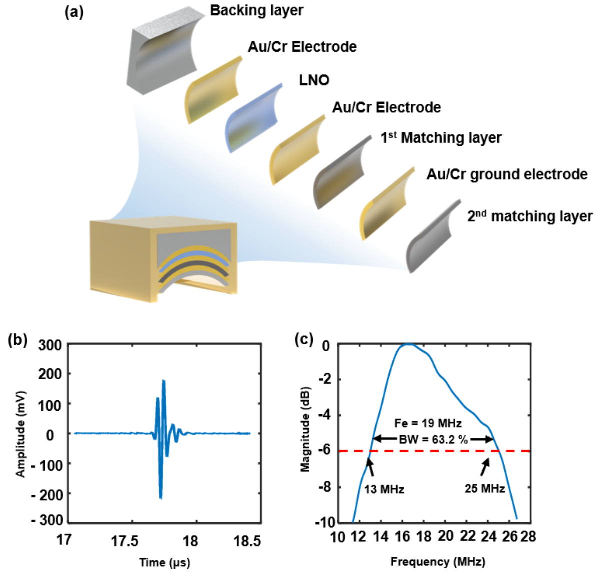

Fig. 2 Characterization of the single-element ultrasonic transducer. (a) Schematic and exploded view of the single-element ultrasonic transducer. (b) Pulse-echo (two-way) waveform measured from the transducer. (c) FFT spectrum of the pulse-echo signal, indicating the −6 dB two-way bandwidth of the transducer.

D. MOR-PAM Reconstruction

In MOR-PAM, the mixed PA signal we acquired is a linear combination of PA signals from individual focal spots. This approach simplifies the model by limiting the excitation to only eight focal spots, where the point sources are positioned close to the virtual detection surface. Consequently, the transducer responses at these eight positions can be linearly combined to reconstruct the mixed PA signal in MOR-PAM, which can be mathematically expressed as

$$p_{m_1',m_2}(t) = \sum_{k=1}^{K} p_{0,(k-1)M_1'+m_1',m_2} h_k\left(t - \frac{d-d_c}{c}\right), \quad (1)$$
$$m_1' = 1,2,\ldots,M_1', m_2 = 1,2,\ldots,M_2, t \geq 0.$$

Here, c is the speed of sound in water, and K is the number of focal spots. In this study, we use 8 focal spots (i.e., K=8). These K focal spots are distributed along the x direction of the coordinate system used in this study. We denote the number of translation locations along the x axis as M_1', leading to a total number of pixels along the x axis as $M_1 = KM_1'$. As shown in Fig. 1d, d and d_c represent the distances between the object plane and the nearest surface of the object to the acoustic mask during imaging and calibration, respectively. Along the y axis, M_2 denotes the number of B scans. We let p_{0,m_1,m_2} be the initial pressure of the pixel with indexes m_1 and m_2 along x and y

Authorized licensed use limited to: CALIFORNIA INSTITUTE OF TECHNOLOGY. Downloaded on December 16,2025 at 17:50:50 UTC from IEEE Xplore. Restrictions apply.
© 2025 IEEE. All rights reserved, including rights for text and data mining and training of artificial intelligence and similar technologies. Personal use is permitted, but republication/redistribution requires IEEE permission. See https://www.ieee.org/publications/rights/index.html for more information.

This article has been accepted for publication in IEEE Transactions on Medical Imaging. This is the author's version which has not been fully edited and content may change prior to final publication. Citation information: DOI 10.1109/TMI.2025.3643618

axes, respectively. The transducer's response to the k-th ($k = 1,2, \dots 8$) focal spot is $h_k(t)$ in the calibration. The signals detected by the transducer for the m_1'-th ($m_1' = 1,2, \dots, M_1'$) translation location in the m_2-th ($m_2 = 1,2, \dots, M_2$) B scan is $p_{m_1',m_2}(t)$.

To ensure accurate reconstruction, we rely on calibrating the system at these eight locations. One possible approach is to directly calibrate each of the eight focal spots. However, any misalignment between the calibrated and actual focal positions may introduce errors. Since full-plane calibration is not performed in MOR-PAM, we adopt an alternative approach: approximating the responses of actual focal spots by introducing small time delays to the signals obtained at the calibrated positions.

This approximation is valid under the condition that, for each focal point, after shifting its distance to the mask surface from d_c to d, a single value of $d-d_c$ can be used to compensate for variations in the acoustic path length from the focal point to all points on the mask surface, i.e., the difference between $d-d_c$, and these path length variations are much smaller than the central wavelength.

For the setup used in this study, $d-d_c \approx 1.2$ µm is used to produce Fig. 6a. This ensures that the transducer response at these positions remains effectively unchanged, allowing us to reconstruct the PA signal with high fidelity.

Further, we discretize the forward model as

$$\mathbf{p} = \mathbf{H}\mathbf{p}_0. \tag{2}$$

Here, the vector $\mathbf{p}_0$ is formed by the initial pressures of the M_1M_2 pixels, the vector $\mathbf{p}$ is formed by discretized signals (L time steps) detected by the transducer at $M_1'M_2$ locations and $\mathbf{H}$ represents the system matrix of shape $M_1'M_2L \times M_1M_2$.i

Given a set of detected signals in $\hat{\mathbf{p}}$, the image can be reconstructed by solving a regularized minimization problem

$$\hat{\mathbf{p}}_0 = \underset{\mathbf{p}_0 \in \mathbb{R}^{M_1M_2}, \mathbf{p}_0 \geq \mathbf{0}}{\operatorname{argmin}} \|\mathbf{H}\mathbf{p}_0 - \hat{\mathbf{p}}\|^2 + \lambda|\mathbf{p}_0|_{\mathrm{TV}} \tag{3}$$

Here, $|\mathbf{p}_0|_{\mathrm{TV}}$ denotes the total variation (TV) of the 2D image corresponding to $\mathbf{p}_0$, and λ is the regularization parameter. TV regularization aids in transforming an image into a new one with piecewise smoother structures, essentially constituting a form of sparseness. Numerically, we solve this optimization problem through a FISTA algorithm [24]. We chose an iteration number of 6 for the FISTA algorithm, considering the trade-off between the image reconstruction quality and time. We chose this option based on experiments that evaluated how varying iteration numbers affected image quality and reconstruction time. The regularization parameter λ was empirically set based on visual evaluation of reconstruction quality under different values. The chosen value provided a stable balance between noise suppression and structural preservation, and consistently yielded satisfactory results without noticeably degrading the lateral resolution.

III. RESULT

A. Numerical simulations of acoustic mask

We used K-wave to model the signals acquired by a cylindrical focused transducer with an acoustic mask. It builds on a simplified version of the 2D sensor mask example in the K-wave MATLAB package with a homogeneous medium [30].
In the simulation, the ultrasonic transducer has a central frequency of 20 MHz. Its one-way bandwidth is 89%, and the aperture diameter is 14 mm. In the simulation, the ultrasonic transducers have a central frequency of 20 MHz. Its one-way bandwidth is 89%, and the aperture diameter is 14 mm. We simulate the medium with two components: an acoustic mask and water for the propagation space. The initial sound pressure is defined as eight-point sources with an interval of 300 µm, to simulate PA signals generated by eight focused spots on the focal plane in MOR-PAM. Therefore, the propagation path of the PA wave and the encoded signal detected by a focused transducer can be obtained.

We chose to use a ladder-shaped model for the acoustic mask. The step design is intended to align with the experimental setup. The mask's varying thickness introduces a spatially dependent delay in the incident PA wavefront. Consequently, the emitted spherical wavefront becomes distorted in a manner that depends on each focal point's position relative to the acoustic mask. This mechanism causes the eight received waveforms to differ significantly compared to the case without the mask. As shown in Fig. 3a, we simulated acoustic masks with a mini-ladder structure, varying the step width from 0.1 mm to 0.8 mm and the step height from 0.1 mm to 0.6 mm. For each mask configuration, eight signals were generated, and the mean correlation coefficient among these signals was computed. The simulation results in Fig. 3b indicate that the lowest mean correlation coefficient occurs when the mini-ladder step width is 0.6 mm and the step height is 0.2 mm, suggesting these as the optimal parameters.

Based on these parameters, we determined the corresponding encoding acoustic mask and simulated the ultrasound propagation process for eight PA point source signals before and after passing through the mask. In Fig. 4a, there is no mask, showing overlapping PA signals from 8 point sources. Fig. 4b, with an optimized acoustic mask, depicts encoded PA signals of the same 8 PA point sources, which show different profiles due to the spatial encoding. Among the 8 encoded PA signals, the mean correlation coefficient decreased significantly to 0.37.

Authorized licensed use limited to: CALIFORNIA INSTITUTE OF TECHNOLOGY. Downloaded on December 16,2025 at 17:50:50 UTC from IEEE Xplore. Restrictions apply.
© 2025 IEEE. All rights reserved, including rights for text and data mining and training of artificial intelligence and similar technologies. Personal use is permitted, but republication/redistribution requires IEEE permission. See https://www.ieee.org/publications/rights/index.html for more information.

This article has been accepted for publication in IEEE Transactions on Medical Imaging. This is the author's version which has not been fully edited and content may change prior to final publication. Citation information: DOI 10.1109/TMI.2025.3643618

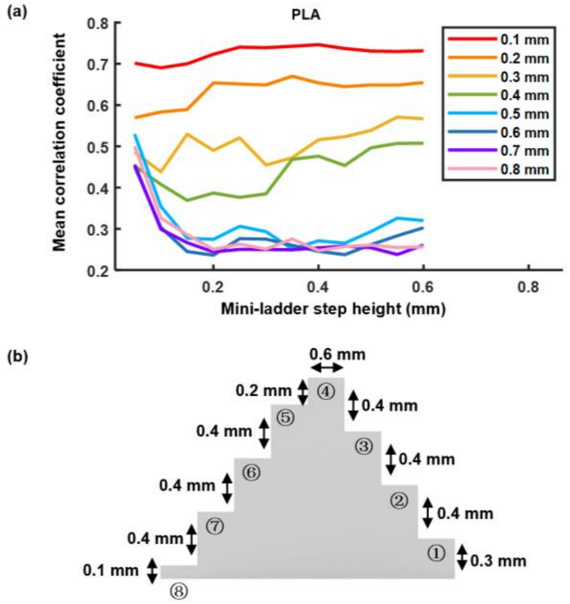

Fig. 3 Optimization of acoustic mask parameters via K-wave Simulation. (a) K-wave simulation result of mean correlation coefficient for different mini-ladder step heights and widths in the acoustic mask. (b) Design parameters of the acoustic mask. Each mini-ladder step has a width of 0.6 mm.

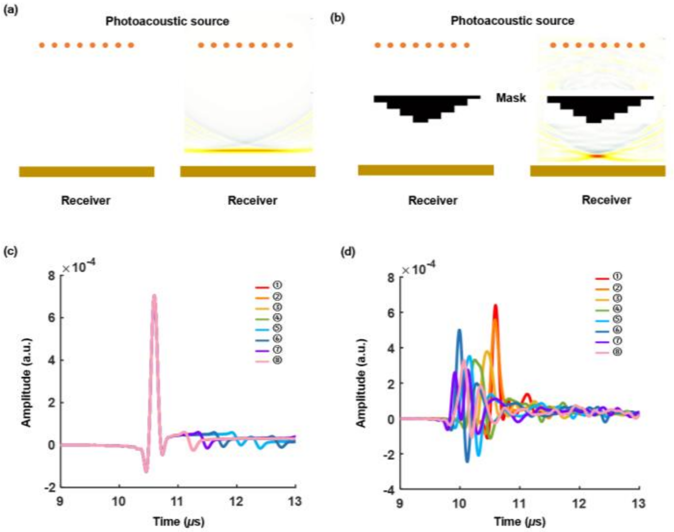

Fig. 4 2D encoding acoustic mask simulations. (a) 8 PA point sources received by a cylindrically focused ultrasonic transducer. (b) 8 PA point sources with an encoding acoustic mask received by a single-element ultrasonic transducer. (c) PA signals generated in (a). (d) PA signals generated in (b). In Fig. 4a and Fig. 4b, the left panel shows the acoustic field distribution at $t = 0$, while the right panel illustrates the acoustic field distribution when the acoustic wave is about to reach the ultrasound transducer.

To provide quantitative context for the encoding–decoding performance, we further conducted a simulation using the optimized mask parameters identified in Fig. 3. Synthetic encoding signals were generated and applied to a 400 × 200 pixel target image, corresponding to a 4 mm × 2 mm field of view with a pixel size of 10 μm (Fig. 5 (c)). The images were reconstructed under varying noise levels and degrees of multiplexing (Fig. 5). Specifically, Fig. 5 (a) and Fig. 5 (b) use eight encodings with 5 dB and 10 dB additive Gaussian noise, respectively, while Fig. 5 (c) uses sixteen encodings with 10 dB noise.

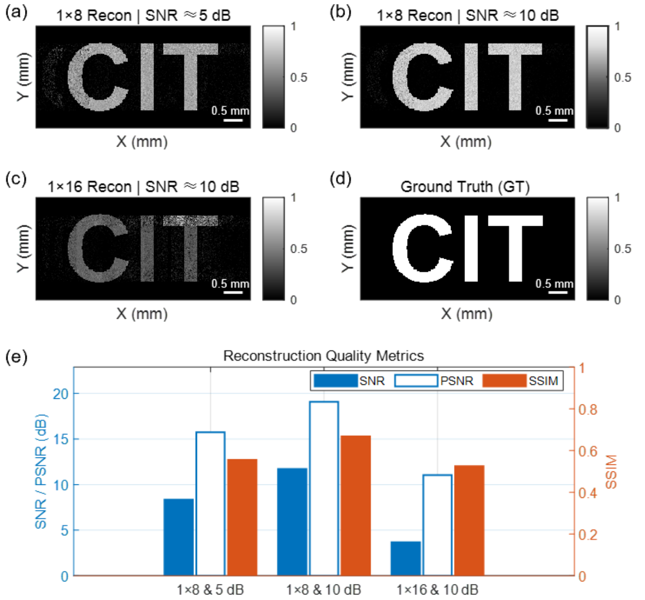

Fig. 5. Simulation-based evaluation of reconstruction quality under noise and multiplexing. (a) Reconstruction with eight encoding signals and 5 dB noise. (b) Reconstruction with eight encoding signals and 10 dB noise. (c) Reconstruction with sixteen encoding signals (same mask) and 10 dB noise. (d) Ground truth (GT). (e) Quality metrics for (a–c): SNR and PSNR (left axis, dB) and SSIM (right axis, 0–1). Reconstructions in (a–c) use simulated encoding signals generated from the mask parameters selected in Fig. 3.

We report SNR, PSNR, and SSIM against the ground truth, after normalizing all reconstructed images to the 0–1 range defined by the ground truth values (Fig. 5e). The results quantify reconstruction fidelity as a function of noise and channel count: increasing the number of concurrent encoding points, under fixed fluence and identical mask, can lower per-spot SNR and increase inter-channel mixing, thereby reducing fidelity. These effects can be mitigated by tailoring the mask to the intended point count to further reduce column correlation in the system matrix and improve conditioning, or by scaling excitation when permissible.

B. Characterization of acoustic mask

According to the simulation results, we designed and fabricated an encoding acoustic mask through 3D printing, with the key parameters illustrated in Fig. 5a. For our calibration procedure, we scanned a human hair phantom with a step size of 0.01 mm. During the scanning, the hair was only illuminated by one focal spot at a time. We extracted the A-line signals from these eight focal positions to form the base system matrix $\mathbf{H}$. It is equivalent to 8 virtual transducers for 2D reconstruction, while the system matrix is independent of the object. For reconstruction, when laser pulses illuminated object with 8 focal spots, the generated PA signals would be equivalent to the linear combination of these virtual transducers. We developed a FISTA algorithm to reconstruct the initial pressure in the 2D volume (Methods).

To quantify the mask's influence on signal transmission, photoacoustic (PA) waveforms generated at absorbers and

Authorized licensed use limited to: CALIFORNIA INSTITUTE OF TECHNOLOGY. Downloaded on December 16,2025 at 17:50:50 UTC from IEEE Xplore. Restrictions apply.
© 2025 IEEE. All rights reserved, including rights for text and data mining and training of artificial intelligence and similar technologies. Personal use is permitted, but republication/redistribution requires IEEE permission. See https://www.ieee.org/publications/rights/index.html for more information.

This article has been accepted for publication in IEEE Transactions on Medical Imaging. This is the author's version which has not been fully edited and content may change prior to final publication. Citation information: DOI 10.1109/TMI.2025.3643618

recorded by a 20 MHz focused ultrasonic transducer were measured under uncoded and coded configurations. As shown in Fig. 6a (without mask) and Fig. 6b (with mask), the mean RMS amplitude across the eight channels decreased slightly from 214 mV to 210 mV, corresponding to a 0.3–3.8% reduction (0.04–0.34 dB) over the 0.1–1.5 mm thickness range. Across this range, the total RMS energy loss was less than 2 dB, indicating that the mask preserved the majority of the signal energy necessary for reliable encoding and reconstruction. Slight amplitude variations among individual channels (e.g., #5 and #6 in Fig. 6b) are attributed to local constructive interference and channel-dependent sensitivity of the transducer, rather than measurement error.

Compared to the acoustical encoding schemes with long propagation and high attenuation [24], our encoding method has less than 2 dB loss due to the PLA mask, which is acceptable for high-frequency photoacoustic detection.

To evaluate the acoustic mask's encoding performance, system matrices with and without mask coding were analyzed. The uncoded configuration (Fig. 6a) demonstrated strong inter-signal correlations among eight PA point sources (mean coefficient: 0.81 (Fig. 6c)), whereas mask coding (Fig. 6b) reduced this value to 0.27 (Fig. 6d), enabling better signal separation. The wavefront variations between experimental results (Fig. 6) and simulations (Fig. 4) could be attributed to inherent model-experiment discrepancies. The 2D simulation may not fully account for 3D wave propagation effects observed experimentally. Additionally, potential mismatches between simulated acoustic parameters (e.g., assumed sound speed and density) and real tissue properties might further influence wavefront morphology through altered propagation dynamics and medium-dependent attenuation behaviors.

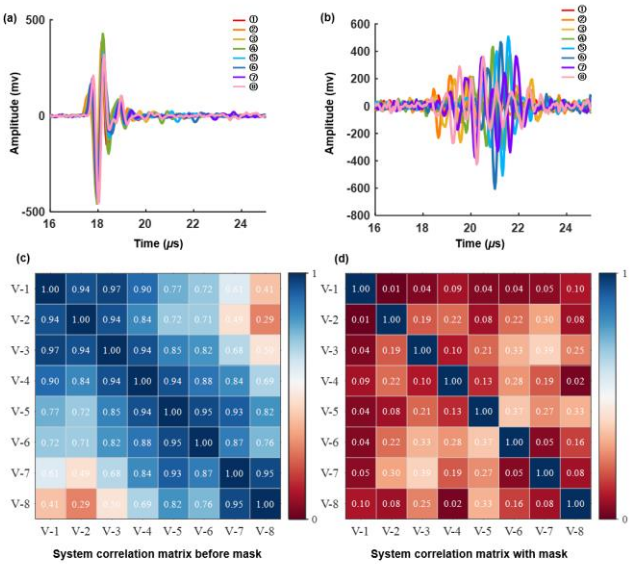

	V-1	V-2	V-3	V-4	V-5	V-6	V-7	V-8
V-1	1.00	0.94	0.97	0.90	0.77	0.72	0.61	0.41
V-2	0.94	1.00	0.94	0.84	0.72	0.71	0.49	0.29
V-3	0.97	0.94	1.00	0.94	0.85	0.82	0.68	0.50
V-4	0.90	0.84	0.94	1.00	0.94	0.88	0.84	0.69
V-5	0.77	0.72	0.85	0.94	1.00	0.95	0.93	0.82
V-6	0.72	0.71	0.82	0.88	0.95	1.00	0.87	0.76
V-7	0.61	0.49	0.68	0.84	0.93	0.87	1.00	0.95
V-8	0.41	0.29	0.50	0.69	0.82	0.76	0.95	1.00

System correlation matrix before mask

	V-1	V-2	V-3	V-4	V-5	V-6	V-7	V-8
V-1	1.00	0.01	0.04	0.09	0.04	0.04	0.05	0.10
V-2	0.01	1.00	0.19	0.22	0.08	0.22	0.30	0.08
V-3	0.04	0.19	1.00	0.10	0.21	0.33	0.39	0.25
V-4	0.09	0.22	0.10	1.00	0.13	0.28	0.19	0.02
V-5	0.04	0.08	0.21	0.13	1.00	0.37	0.27	0.33
V-6	0.04	0.22	0.33	0.28	0.37	1.00	0.05	0.16
V-7	0.05	0.30	0.39	0.19	0.27	0.05	1.00	0.08
V-8	0.10	0.08	0.25	0.02	0.33	0.16	0.08	1.00

System correlation matrix with mask

Fig. 6 Experimental characterization of the 2D coding acoustic mask fabricated. (a) 8 signal responses generated by eight photoacoustic point sources propagate in water without the mask. (b) 8 signal responses generated by eight photoacoustic point sources propagate in water with an acoustic mask. (c) Correlation matrix without the mask. (d) Correlation matrix with the mask.

We further quantified the system matrix by calculating its condition number. Without encoding, the condition number was approximately 23.7, indicating moderate ill-posedness. After introducing the optimized acoustic mask, the condition number decreased to 3.4, confirming a substantial improvement in numerical robustness for reconstruction. These improvements enable accurate and stable reconstruction using total variation regularization within the FISTA algorithm.

C. *Characterization experiment of MOR-PAM*

To experimentally validate the proposed MOR-PAM system, we first imaged a 2D structure fabricated from human hair (~90 μm in diameter). The structure was fixed on the edge of a hollow base and illuminated by eight focused laser spots at 266 nm, with an energy of 180 nJ per pulse. The distance between the sample and the acoustic mask was 15 mm, and the mask was positioned 2 mm in front of the transducer. The scanning step size was 10 μm in both directions parallel and perpendicular to the focal line.

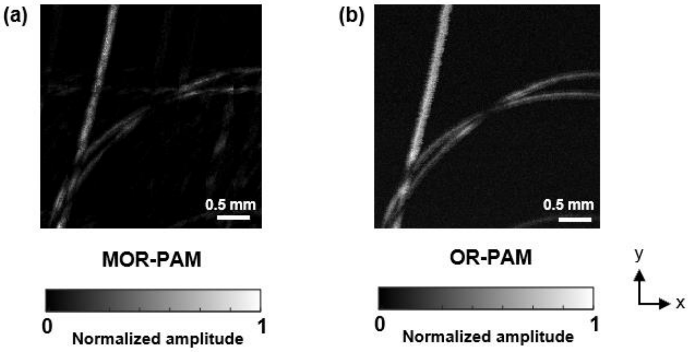

Fig. 7 2D experimental images of a human hair structure phantom. (a) 2D Maximum-amplitude projection image acquired with MOR-PAM. (b) 2D Maximum-amplitude projection image acquired with traditional OR-PAM. Norm., normalized.

Using MOR-PAM, we acquired a 3.6 mm × 3.59 mm image within approximately 6 s, whereas conventional OR-PAM under identical laser repetition rate and step size required about 50 s. Fig. 7a shows the XY-plane maximum-amplitude projection of the human-hair phantom reconstructed from multiplexed signals, and Fig. 7b shows the corresponding result from conventional OR-PAM. The MOR-PAM reconstruction clearly recovered the hair features, confirming the validity of the spatial encoding and decoding process. The slight image degradation observed in Fig. 7a is attributed to imperfect signal separation during multiplexed acquisition, which lowers the effective SNR compared with single-focus scanning.

Authorized licensed use limited to: CALIFORNIA INSTITUTE OF TECHNOLOGY. Downloaded on December 16,2025 at 17:50:50 UTC from IEEE Xplore. Restrictions apply.
© 2025 IEEE. All rights reserved, including rights for text and data mining and training of artificial intelligence and similar technologies. Personal use is permitted, but republication/redistribution requires IEEE permission. See https://www.ieee.org/publications/rights/index.html for more information.

This article has been accepted for publication in IEEE Transactions on Medical Imaging. This is the author's version which has not been fully edited and content may change prior to final publication. Citation information: DOI 10.1109/TMI.2025.3643618

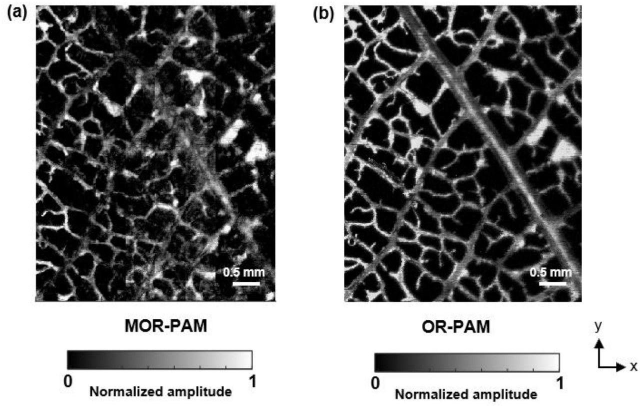

Fig. 8 2D experimental images of a leaf skeleton phantom. (a) 2D Maximum-amplitude projection image acquired with MOR-PAM. (b) 2D Maximum-amplitude projection image acquired with traditional OR-PAM. Norm., normalized.

To further demonstrate the system's capability in reconstructing more complex spatial patterns, we performed an additional experiment on a leaf skeleton phantom**.** The same imaging configuration was used as in the hair phantom experiment. As shown in Fig. 8a, the MOR-PAM reconstruction successfully revealed the dense, vessel-like network of the leaf skeleton, while Fig. 8b presents the corresponding result obtained by conventional OR-PAM. Although minor artifacts are present, the overall structure is faithfully reproduced, verifying that the proposed method remains robust when imaging intricate, non-sparse samples.

IV. CONCLUSION AND DISCUSSION

In summary, we demonstrated that an acoustic mask enables a single-element transducer to perform parallel detection of multiple focal spots, thereby accelerating OR-PAM. The plastic mask introduces location-dependent phase in the ultrasound field and causes each PA signal to be uniquely identifiable within the mixed PA signal, which are linear combinations of the PA signals from individual spots. Our MOR-PAM system enhances imaging speed by eightfold compared to the traditional OR-PAM approach, while incurring only marginal additional costs to the system (i.e., 3D-printed PLA mask). The extent of improvement depends on the number of effective spots formed by the DOE, which can be further increased if the laser power is sufficient. The MOR-PAM method was successfully demonstrated experimentally via imaging of a phantom made by human hairs and leaf skeleton phantom. The experiments show a lateral resolution of 3 µm. To achieve better lateral resolution, we can further increase the numerical aperture.

To optimize the imaging performance of our system, we have devised an enhanced regularization algorithm for the effective separation of mixed signals. Through simulations, this method has demonstrated its capability to successfully separate and reconstruct up to 8 mixed signals, each having an SNR of ~10. Moreover, its proficiency in decomposing mixed signals has been experimentally confirmed using our MOR-PAM system. The main challenge in our current implementation is the difficulty of illuminating the imaged objects in reflection mode due to the opaque coding mask and acoustic transducer, which will affect the optical focusing. To enable coaxial optical and acoustic access for reflection-mode imaging, future iterations of our system may overcome this limitation by incorporating optically transparent optical–acoustic combiners [31].

In this study, we used a hair phantom and leaf skeleton phantom to validate the feasibility of the proposed system. While these samples were suitable for demonstrating core system performance, future studies will focus on histological sections and biologically heterogeneous tissues to more comprehensively assess the system's imaging capabilities in realistic biomedical settings.

At present, one major limitation of ultraviolet photoacoustic microscopy (UV-PAM) using 266 nm excitation is the inherently low pulse repetition rate of available lasers (i.e., 10–20 kHz), which severely constrains imaging throughput. Consequently, UV-PAM systems based on 266 nm excitation will greatly benefit from parallelized acquisition strategies. This is in contrast to more commonly used 532 nm lasers, which has been demonstrated at 1–2 MHz for PAM [32]. It is worth mentioning that although we demonstrated MOR-PAM at 266 nm, the method can be easily adapted to other wavelengths such as 532 nm for vascular or tumor imaging in vivo.

Moreover, with sufficient laser energy and robust encoding, the number of focal spots can also be further increased. In current system, a 180 nJ pulse shared by 8 foci (~22.5 nJ per spot) yields reconstructed signals with an SNR of 10–14 dB. In principle, a 100 µJ laser could sustain ~200 foci at a comparable SNR. For future scalability, a two-dimensional DOE could be used to generate grid-patterned focal arrays. However, increasing the number of focal spots may lead to stronger inter-signal correlations and thus more ill-posed inversion problems. To maintain signal separability and reconstruction stability in such configurations, advanced encoding strategies and regularized or data-driven reconstruction algorithms will be explored.

Our work brings new opportunities not only for UV-PAM techniques but also for all the OR-PAM for biological and biomedical applications where high-speed imaging is needed. We use an acoustic mask and a single-element cylindrical focused transducer for multifocal UV-PAM imaging. By simulation and experiment, we demonstrate that our method can boost the PAM imaging speed limited by the laser repetition rate. We believe that this approach will provide new opportunities for high-resolution PAM applications. Our device can also extend to applications like minimally invasive imaging catheters, overcoming the limitations of thin form factors for accommodating numerous ultrasound arrays in rapid optical resolution photoacoustic endoscopes. Here, we demonstrated experimentally that a simple setup with a coding mask enables parallel PA imaging without complexity hardware. This technique holds promise for advancing high-resolution PAM applications.

DATA AVAILABILITY

The data supporting the findings of this study are provided

Authorized licensed use limited to: CALIFORNIA INSTITUTE OF TECHNOLOGY. Downloaded on December 16,2025 at 17:50:50 UTC from IEEE Xplore. Restrictions apply.
© 2025 IEEE. All rights reserved, including rights for text and data mining and training of artificial intelligence and similar technologies. Personal use is permitted, but republication/redistribution requires IEEE permission. See https://www.ieee.org/publications/rights/index.html for more information.

This article has been accepted for publication in IEEE Transactions on Medical Imaging. This is the author's version which has not been fully edited and content may change prior to final publication. Citation information: DOI 10.1109/TMI.2025.3643618

within the Article. The raw and analyzed datasets generated during the study are available for research purposes from the corresponding authors upon reasonable request.

ACKNOWLEDGMENT

L.V.W. has a financial interest in Microphotoacoustics, Inc., CalPACT, LLC, and Union Photoacoustic Technologies, Ltd., which, however, did not support this work. The authors gratefully acknowledge the TechLab at Caltech for providing 3D printing services.

REFERENCES

[1] R. Cao, S. D. Nelson, S. Davis, Y. Liang, Y. L. Luo, Y. D. Zhang, B. Crawford, and L. H. V. Wang, "Label-free intraoperative histology of bone tissue via deep-learning-assisted ultraviolet photoacoustic microscopy," *Nature Biomedical Engineering*, pp. 124-134, Sep 19, 2022.

[2] Z. Qu, C. Liu, J. Zhu, Y. Zhang, Y. Zhou, and L. Wang, "Two-step proximal gradient descent algorithm for photoacoustic signal unmixing," *Photoacoustics,* vol. 27, pp. 100379, Sep, 2022.

[3] J. Shi, T. T. W. Wong, Y. He, L. Li, R. Zhang, C. S. Yung, J. Hwang, K. Maslov, and L. V. Wang, "High-resolution, high-contrast mid-infrared imaging of fresh biological samples with ultraviolet-localized photoacoustic microscopy," *Nat Photonics,* vol. 13, pp. 609-615, Sep, 2019.

[4] T. T. W. Wong, R. Zhang, C. Zhang, H. C. Hsu, K. I. Maslov, L. Wang, J. Shi, R. Chen, K. K. Shung, Q. Zhou, and L. V. Wang, "Label-free automated three-dimensional imaging of whole organs by microtomy-assisted photoacoustic microscopy," *Nat Commun,* vol. 8, no. 1, pp. 1386, Nov 9, 2017.

[5] L. Wang, C. Zhang, and L. V. Wang, "Grueneisen relaxation photoacoustic microscopy," *Phys Rev Lett,* vol. 113, no. 17, pp. 174301, Oct 24, 2014.

[6] W. R. Pang, B. W. Zhu, H. H. Li, Y. Y. Zhou, C. M. Woo, X. Z. Huang, T. T. Zhong, H. Lo, L. Y. Wang, P. X. Lai, and L. M. Nie, "Direct Monitoring of Whole-Brain Electrodynamics via High-Spatiotemporal-Resolution Photoacoustics with Voltage-Sensitive Dye." Laser & Photonics Reviews, vol. 18, no. 10, May 23, 2024.

[7] Y. He, J. Shi, K. I. Maslov, R. Cao, and L. V. Wang, "Wave of single-impulse-stimulated fast initial dip in single vessels of mouse brains imaged by high-speed functional photoacoustic microscopy," *J Biomed Opt,* vol. 25, no. 6, pp. 1-11, Jun, 2020.

[8] C. Yeh, J. Liang, Y. Zhou, S. Hu, R. E. Sohn, J. M. Arbeit, and L. V. Wang, "Photoacoustic microscopy of arteriovenous shunts and blood diffusion in early-stage tumors," *J Biomed Opt,* vol. 21, no. 2, pp. 20501, Feb, 2016.

[9] K. Wang, C. Li, R. Chen, and J. Shi, "Recent advances in high-speed photoacoustic microscopy," *Photoacoustics,* vol. 24, pp. 100294, Dec, 2021.

[10] S.-W. Cho, S. M. Park, B. Park, D. Y. Kim, T. G. Lee, B.-M. Kim, C. Kim, J. Kim, S.-W. Lee, and C.-S. Kim, "High-speed photoacoustic microscopy: A review dedicated on light sources," *Photoacoustics,* vol. 24, 2021.

[11] J. Yao, L. Wang, J.-M. Yang, K. I. Maslov, T. T. W. Wong, L. Li, C.-H. Huang, J. Zou, and L. V. Wang, "High-speed label-free functional photoacoustic microscopy of mouse brain in action," *Nature Methods,* vol. 12, no. 5, pp. 407-410, 2015.

[12] H. Assi, R. Cao, M. Castelino, B. Cox, F. J. Gilbert, J. Grohl, K. Gurusamy, L. Hacker, A. M. Ivory, J. Joseph, F. Knieling, M. J. Leahy, L. Lilaj, S. Manohar, I. Meglinski, C. Moran, A. Murray, A. A. Oraevsky, M. D. Pagel, M. Pramanik, J. Raymond, M. K. A. Singh, W. C. Vogt, L. Wang, S. Yang, I. Members Of, and S. E. Bohndiek, "A review of a strategic roadmapping exercise to advance clinical translation of photoacoustic imaging: From current barriers to future adoption," *Photoacoustics,* vol. 32, pp. 100539, Aug, 2023.

[13] X. Liu, T. T. W. Wong, J. Shi, J. Ma, Q. Yang, and L. V. Wang, "Label-free cell nuclear imaging by Gruneisen relaxation photoacoustic microscopy," *Opt Lett,* vol. 43, no. 4, pp. 947-950, Feb 15, 2018.

[14] Q. Chen, H. Guo, T. Jin, W. Qi, H. Xie, and L. Xi, "Ultracompact high-resolution photoacoustic microscopy," *Opt Lett,* vol. 43, no. 7, pp. 1615-1618, Apr 1, 2018.

[15] J. Chen, Y. Zhang, S. Bai, J. Zhu, P. Chirarattananon, K. Ni, Q. Zhou, and L. Wang, "Dual-foci fast-scanning photoacoustic microscopy with 3.2-MHz A-line rate," *Photoacoustics,* vol. 23, pp. 100292, Sep, 2021.

[16] Z. Chen, A. Ozbek, J. Rebling, Q. Zhou, X. L. Dean-Ben, and D. Razansky, "Multifocal structured illumination optoacoustic microscopy," *Light Sci Appl,* vol. 9, pp. 152, 2020.

[17] J. Xia, G. Li, L. Wang, M. Nasiriavanaki, K. Maslov, J. A. Engelbach, J. R. Garbow, and L. V. Wang, "Wide-field two-dimensional multifocal optical-resolution photoacoustic-computed microscopy," *Optics Letters,* vol. 38, no. 24, 2013.

[18] H. Wan, Y. Zhou, L. Ying, J. Meng, L. Song, and J. Xia, "Enabling high-speed wide-field dynamic imaging in multifocal photoacoustic computed microscopy: a simulation study," *Appl Opt,* vol. 55, no. 14, pp. 3724-9, May 10, 2016.

[19] B. T. Cox, and P. C. Beard, "Photoacoustic tomography with a single detector in a reverberant cavity," *Journal of the Acoustical Society of America,* vol. 125, no. 3, pp. 1426-1436, Mar, 2009.

[20] M. D. Brown, E. Z. Zhang, B. E. Treeby, P. C. Beard, and B. T. Cox, "Reverberant cavity photoacoustic imaging," *Optica,* vol. 6, no. 6, pp. 821-822, Jun 20, 2019.

[21] Y. Li, T. T. W. Wong, J. H. Shi, H. C. Hsu, and L. H. V. Wang, "Multifocal photoacoustic microscopy using a single-element ultrasonic transducer through an ergodic relay," *Light-Science & Applications,* vol. 9, no. 1, Jul 31, 2020.

[22] G. Montaldo, D. Palacio, M. Tanter, and M. Fink, "Time reversal kaleidoscope: A smart transducer for three-dimensional ultrasonic imaging," *Applied Physics Letters,* vol. 84, no. 19, pp. 3879-3881, May 10, 2004.

[23] G. Montaldo, D. Palacio, M. Tanter, and M. Fink, "Building three-dimensional images using a time-reversal chaotic cavity," *Ieee Transactions on Ultrasonics Ferroelectrics and Frequency Control,* vol. 52, no. 9, pp. 1489-1497, Sep, 2005.

[24] Y. Zhang, P. Hu, L. Li, R. Cao, A. Khadria, K. Maslov, X. Tong, Y. Zeng, L. Jiang, Q. Zhou, and L. V. Wang, "Ultrafast longitudinal imaging of haemodynamics via single-shot volumetric photoacoustic tomography with a single-element detector," *Nat Biomed Eng*, vol. 8, no. 4, pp. 712-725, Nov 30, 2023.

[25] B. B. Yan, B. Song, G. Mu, Y. B. Fan, and Y. Y. Zhao, "Compressed single-shot 3D photoacoustic imaging with a single-element transducer," *Photoacoustics*, vol. 34, pp. 100570, Dec, 2023.

[26] Y. Y. Zhao, and L. H. V. Wang, "Single-shot photoacoustic imaging with single-element transducer through a spatiotemporal encoder," *J Biomed Opt*, vol. 28, no. 4, pp. 046004, Apr 1, 2023.

[27] R. Cao, J. J. Zhao, L. Li, L. Du, Y. D. Zhang, Y. L. Luo, L. M. Jiang, S. Davis, Q. F. Zhou, A. de la Zerda, and L. H. V. Wang, "Optical-resolution photoacoustic microscopy with a needle-shaped beam," *Nature Photonics,* vol. 17, no. 1, pp. 89-95, Jan, 2023.

[28] R. Cao, Y. Luo, J. Zhao, Y. Zeng, Y. Zhang, Q. Zhou, A. le da Zerda, and L. V. Wang, "Optical-resolution parallel ultraviolet photoacoustic microscopy for slide-free histology," *Sci Adv,* vol. 10, no. 50, pp. eado0518, Dec 13, 2024.

[29] A. Beck, and M. Teboulle, "A Fast Iterative Shrinkage-Thresholding Algorithm for Linear Inverse Problems," *SIAM Journal on Imaging Sciences,* vol. 2, no. 1, pp. 183-202, 2009.

[30] B. E. Treeby, and B. T. Cox, "k-Wave: MATLAB toolbox for the simulation and reconstruction of photoacoustic wave fields," *J Biomed Opt,* vol. 15, no. 2, pp. 021314, Mar-Apr, 2010.

[31] S. Cho, M. Kim, J. Ahn, Y. Kim, J. Lim, J. Park, H. H. Kim, W. J. Kim, and C. Kim, "An ultrasensitive and broadband transparent ultrasound transducer for ultrasound and photoacoustic imaging in-vivo," *Nat Commun*, vol. 15, pp. 1444, Feb 16, 2024.

[32] Y. Z. Liang, L. Jin, B. O. Guan, and L. D. Wang, "2 MHz multi-wavelength pulsed laser for functional photoacoustic microscopy," Optics Letters, pp. 1452-1455, Apr 1, 2017.

Authorized licensed use limited to: CALIFORNIA INSTITUTE OF TECHNOLOGY. Downloaded on December 16,2025 at 17:50:50 UTC from IEEE Xplore. Restrictions apply.
© 2025 IEEE. All rights reserved, including rights for text and data mining and training of artificial intelligence and similar technologies. Personal use is permitted, but republication/redistribution requires IEEE permission. See https://www.ieee.org/publications/rights/index.html for more information.